Electronic Supplementary Information (ESI) for

A Transparent *p*-Type Semiconductor Designed via a Polarizability-Enhanced Strongly Correlated Insulator Oxide Matrix

Seung Yong Lee[1,2†], Inseo Kim[3†], Hyun Jae Kim[1,4†], Sangjun Sim[3], Jae Hoon Lee[3,5], Sora Yun[3], Joonho Bang[6], Kyoung Won Park[4], Chul Jong Han[4], Hyun-Min Kim[7], Heesun Yang[7], Bongjae Kim[8], Seongil Im[9], Antonio Facchetti[10]*, Min Suk Oh[4]*, Kyu Hyoung Lee[1]*, and Kimoon Lee[3,11]*

[1]Department of Materials Science and Engineering, Yonsei University, Seoul 03722, Republic of Korea.
[2]KIURI Institute, Yonsei University, Seoul 03722, Republic of Korea.
[3]Department of Physics, Kunsan National University, Gunsan 54150, Republic of Korea.
[4]Display Research Center, Korea Electronics Technology Institute (KETI), Seongnam 13509, Republic of Korea.
[5]Global Infra Technology, Samsung Electronics, Yongin 17113, Republic of Korea.
[6]School of Materials Science & Engineering, Gyeongsang National University, Jinju 52828, Republic of Korea.
[7]Department of Materials Science and Engineering, Hongik University, Seoul 04066, Republic of Korea.
[8]Department of Physics, Kyungbuk National University, Daegu 41566, Republic of Korea.
[9]Department of Physics, Van der Waals Materials Research Center, Yonsei University, Seoul 03722, Republic of Korea.
[10]School of Materials Science and Engineering, Georgia Institute of Technology, Atlanta, GA 30332, USA.
[11]The Institute of Basic Science, Kunsan National University, Gunsan 54150, Republic of Korea.

†These authors contributed equally to this work.

*Corresponding author: afacchetti6@gatech.edu, ohms@keti.re.kr, khlee2018@yonsei.ac.kr, kimoon.lee@kunsan.ac.kr

S1. Magnetic ground state calculation

By comparing the total energy of the three types of possible magnetic ground states of NiWO$_4$ in Figure S1, the antiferromagnetic (AFM)-ordered state exhibits the lowest energy, i.e. the most stable ground state in NiWO$_4$, a data consistent with our magnetization measurements. (Fig. 2g) [S1]
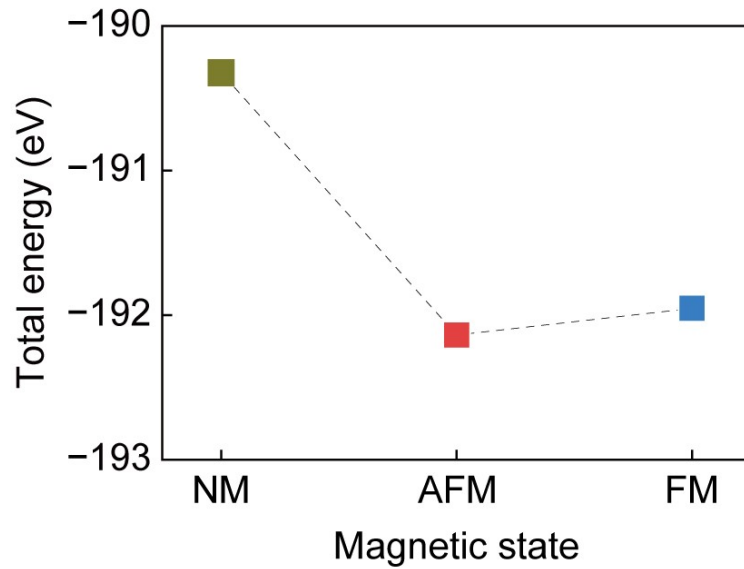

Figure S1. Total energy calculations based on various magnetic ground state for NiWO$_4$. NM and AFM, and FM denote the paramagnetic, antiferromagnetic, and ferromagnetic ground state, respectively.

S2. Quantum dot synthesis

In a typical synthesis of composition-gradient CdZnSeS core quantum dots (QDs) as a green emission layer (EML),[S2] 0.14 mmol of Cd acetate, 3.41 mmol of Zn oxide, and 7 mL of oleic acid (OA) were loaded in a three-neck flask, and the mixture was heated to 150 °C with N_2 flowing. Then, 15 mL of 1-octadecene (ODE) was added into the reaction flask, and the reactor was further heated to 320 °C. At the elevated temperature, an anionic stock solution of 1.76 mmol of Se and 2.64 mmol of S dissolved in 1.85 mL of trioctylphosphine (TOP) was swiftly injected into the above flask, and the reaction proceeded at that temperature for about 20 min. Next, a S-ODE solution consisting of 1.6 mmol of S in 2.4 mL of ODE was introduced into the CdZnSeS QD growth solution and the reaction was held at 310 °C for 8 min. Subsequently, a Zn stock solution, prepared by dissolving 2.86 mmol of Zn acetate dihydrate in 4 mL of OA and 1 mL of ODE was injected, and the reaction temperature was lowered to 275 °C. At last, a S-TOP solution of 9.65 mmol of S dissolved in 5 mL of TOP was introduced in a dropwise fashion. This reaction proceeded at 275 °C for 10 min. As-synthesized CdZnSeS@ZnS QDs were precipitated by adding an excess of ethanol, repeatedly purified with a solvent combination of hexane/ethanol (1/4 in volume ratio) by centrifugation, and finally re-dispersed in toluene for characterization and device fabrication. When we measured the photoluminescence (PL) spectrum of a diluted QD solution (2.25 mg/ml), the peak wavelength, full width at half maximum (FWHM), and internal quantum efficiency were 519.54 nm, 18.98 nm, and 79.72%, respectively.

S3. The powder X-ray diffraction (PXRD) analysis

The PXRD patterns of $Ni_{1-x}Cu_xWO_4$ with various x were measured as shown in Fig. S2. The results of Rietveld refinement are displayed and listed in Fig. S3 and Table S1, respectively. From these results the crystal structure of $Ni_{1-x}Cu_xWO_4$ is shown in Fig. 1a and 1e.
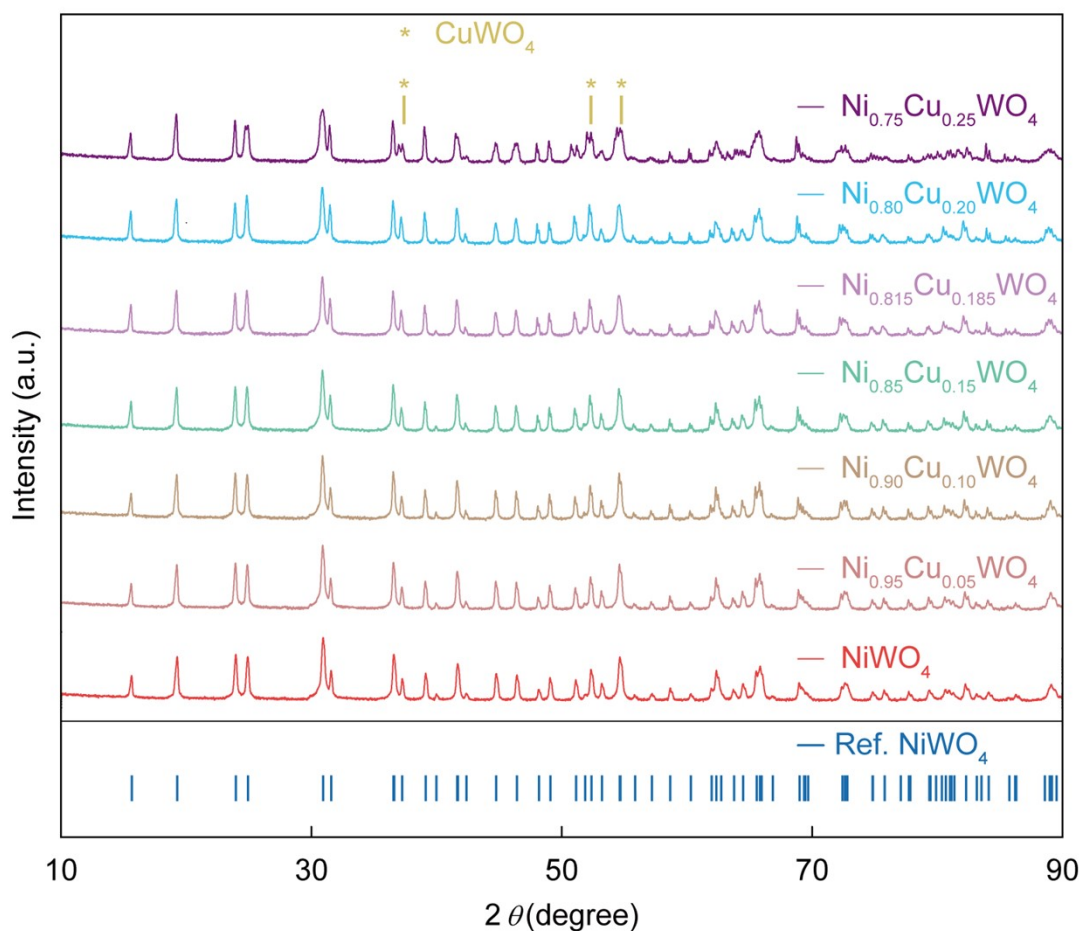

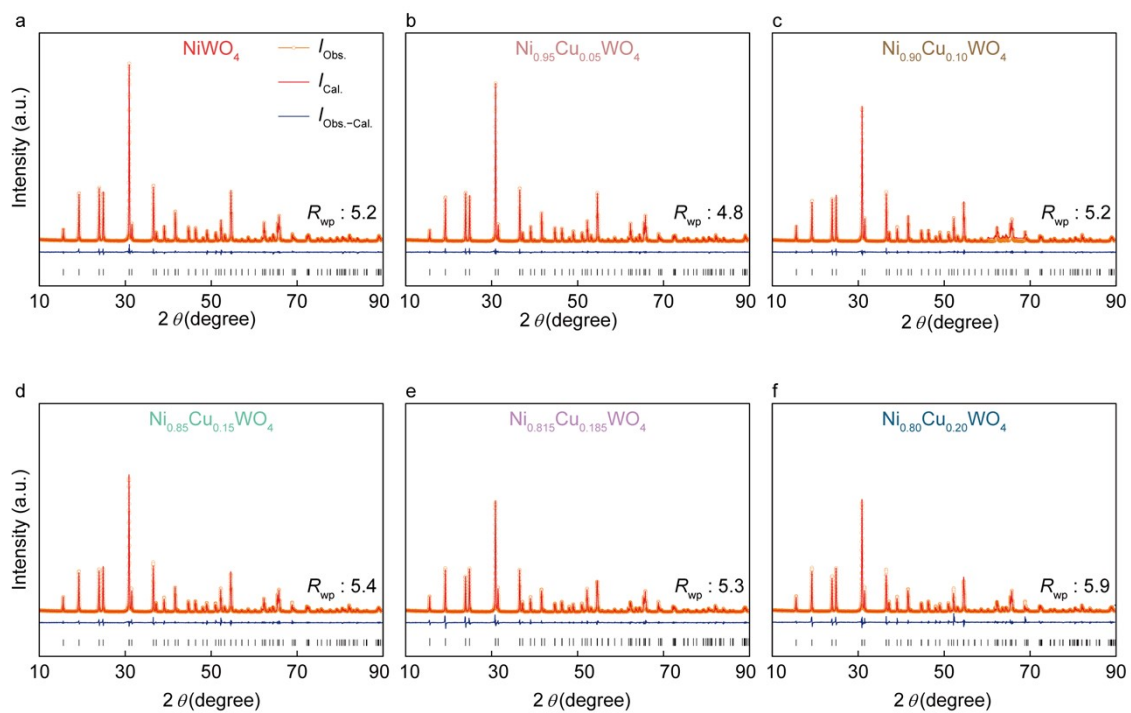**Figure S2.** PXRD patterns of $Ni_{1-x}Cu_xWO_4$ with various Cu contents (x).

Figure S3. Rietveld refinement results for $Ni_{1-x}Cu_xWO_4$ with various x.

Table S1. Detailed parameters obtained by Rietveld refinements for $Ni_{1-x}Cu_xWO_4$.

Composition	$NiWO_4$	$Ni_{0.95}Cu_{0.05}WO_4$	$Ni_{0.90}Cu_{0.10}WO_4$	$Ni_{0.85}Cu_{0.15}WO_4$	$Ni_{0.815}Cu_{0.185}WO_4$	$Ni_{0.80}Cu_{0.20}WO_4$
Space group				P12/c1		
a (Å)	4.603	4.604	4.605	4.606	4.608	4.608
b (Å)	5.666	5.669	5.671	5.673	5.675	5.675
c (Å)	4.911	4.912	4.912	4.913	4.914	4.914
V (Å³)	128.104	128.205	128.285	128.348	128.497	128.509
Atomic coordination & Occupation						
Ni	(0.5, 0.658, 0.25)	(0.5, 0.659, 0.25)	(0.5, 0.659, 0.25)	(0.5 0.660, 0.25)	(0.5 0.657, 0.25)	(0.5, 0.659, 0.25)
	1	0.936	0.899	0.857	0.813	0.805
Cu		(0.5, 0.659 0.25)	(0.5, 0.659, 0.25)	(0.5, 0.660, 0.25)	(0.5, 0.657, 0.25)	(0.5, 0.659, 0.25)
		0.064	0.101	0.143	0.187	0.195
W	(0, 0.178, 0.25)	(0, 0.178, 0.25)	(0, 0.178, 0.25)	(0, 0.179, 0.25)	(0, 0.180, 0.25)	(0, 0.180, 0.25)
O1	(0.218, 0.106, 0.918)	(0.202, 0.102, 0.910)	(0.206, 0.101, 0.915)	(0.187, 0.110, 0.903)	(0.203, 0.101, 0.913)	(0.202, 0.101, 0.915)
O2	(0.267, 0.369, 0.397)	(0.267, 0.372, 0.397)	(0.260, 0.373, 0.399)	(0.260, 0.379, 0.403)	(0.267, 0.370, 0.397)	(0.262, 0.372, 0.400)
R_{wp} (%)	5.222	4.814	5.194	5.372	6.315	5.950

S4. Compositional analysis

The quantitative stoichiometry ratio of Ni and Cu in $Ni_{1-x}Cu_xWO_4$ were measured by inductively coupled plasma mass spectroscopy (ICP-MS). From the atomic composition as listed in Table S2, it can be concluded that the measured stoichiometry is almost identical to those from Rietveld refinement analysis with a negligible deviation as displayed in Fig. 1c.

Table S2. The atomic composition for $Ni_{1-x}Cu_xWO_4$ determined by ICP-MS.

Nominal	Ni	Cu
$NiWO_4$	0.959	0.000
$Ni_{0.95}Cu_{0.05}WO_4$	0.962	0.050
$Ni_{0.90}Cu_{0.10}WO_4$	0.875	0.096
$Ni_{0.85}Cu_{0.15}WO_4$	0.855	0.149
$Ni_{0.815}Cu_{0.185}WO_4$	0.821	0.184
$Ni_{0.80}Cu_{0.20}WO_4$	0.803	0.200

S5. Raman spectra analysis

Full-ranged Raman spectra of $Ni_{1-x}Cu_xWO_4$, corresponding to Fig. 1d, are displayed in Fig. S4. All the peaks were well assigned as the characteristic vibrational modes for monoclinic $NiWO_4$ regardless of x. [S3]
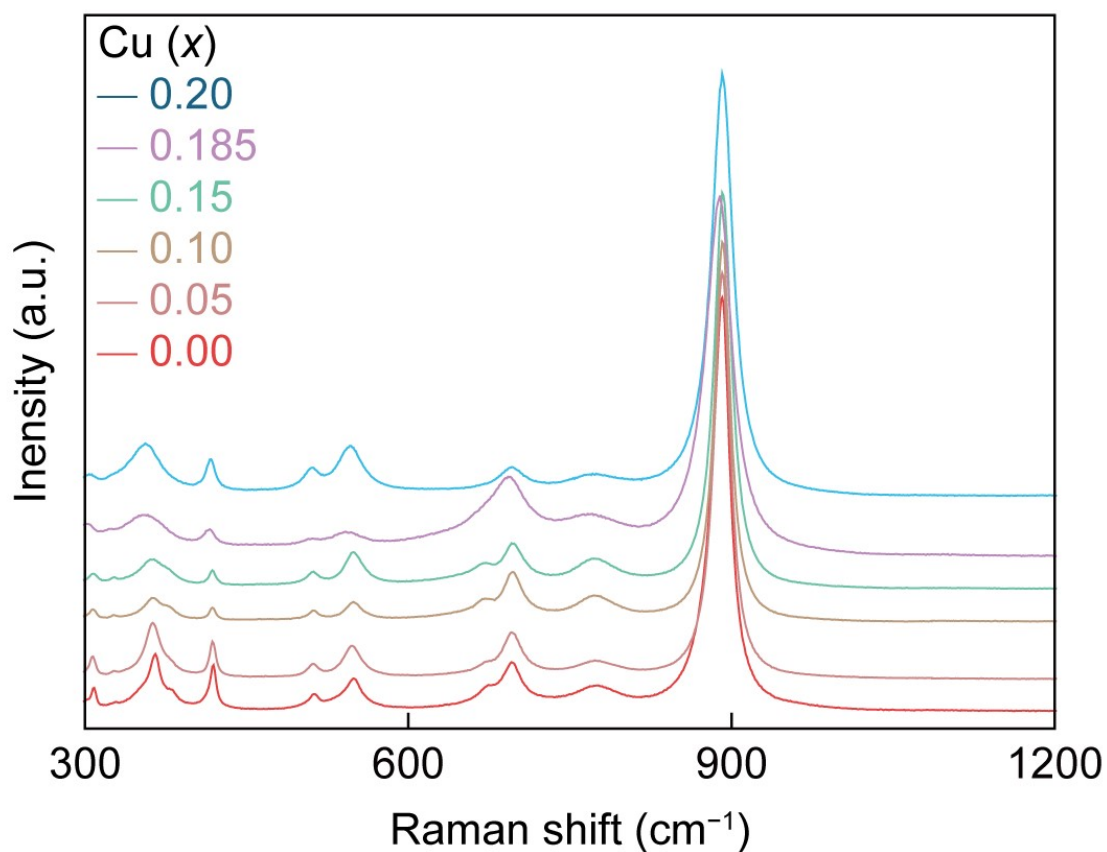

Figure S4. Raman spectra of $Ni_{1-x}Cu_xWO_4$ with various x obtained from 300 to 1200 cm^{-1} wavenumber region.

S6. SEM-EDS element mapping for $Ni_{1-x}Cu_xWO_4$ samples

Figure S5 shows scanning electron microscopy (SEM) – energy dispersive X-ray spectroscopy (EDS) mapping results. From the results, it can be observed that uniform distributions for all elements (Ni, W, O, and Cu) in the synthesized $Ni_{1-x}Cu_xWO_4$ samples for $0 \leq x \leq 0.02$.
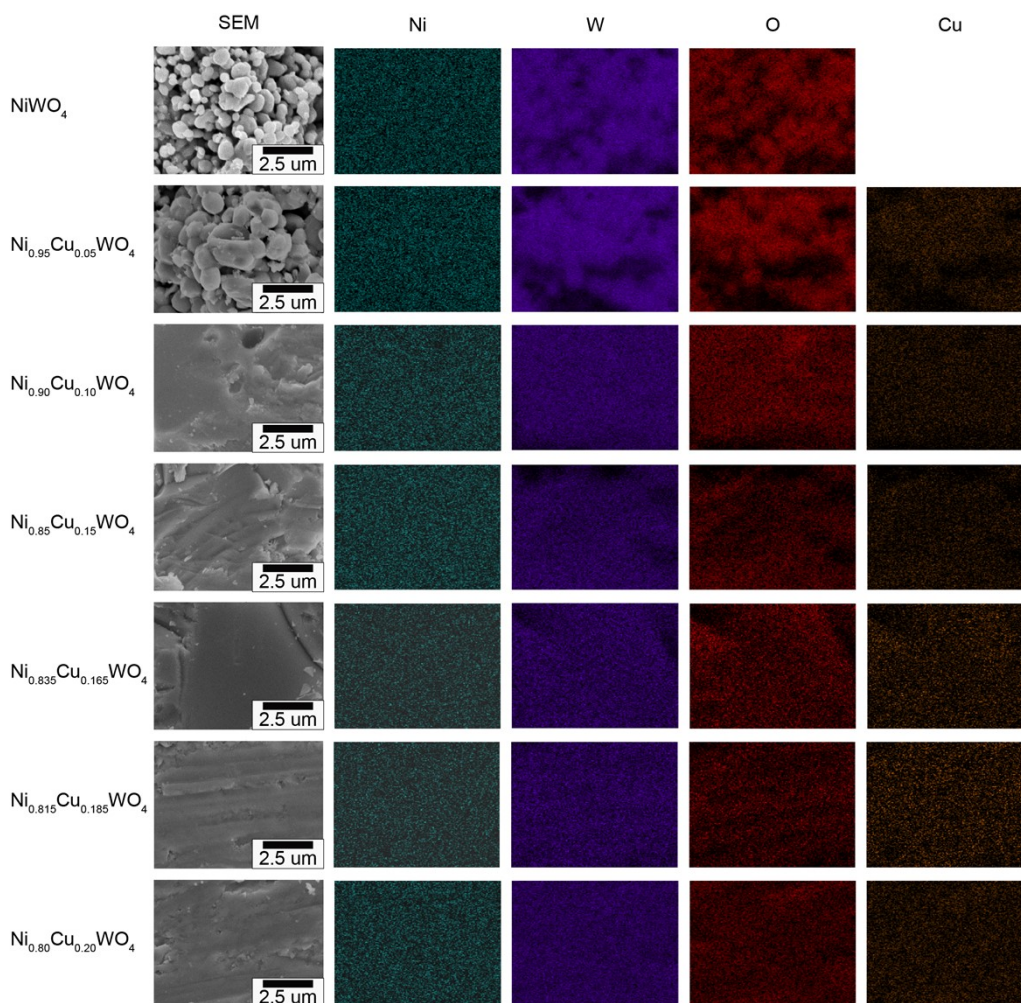

Figure S5. SEM-EDS mapping results for the synthesized $Ni_{1-x}Cu_xWO_4$ samples. ($x = 0$, 0.05, 0.10, 0.15, 0.165, 0.185, and 0.20)

S7. Optical absorption spectra of $Ni_{1-x}Cu_xWO_4$ samples

Figure S6 displays the absorption spectra obtained from the ellipsometry measurements for $Ni_{1-x}Cu_xWO_4$ samples with different x values. To estimate the indirect and direct absorption edges, the absorption coefficients (α's) are converted into $(\alpha h\nu)^{0.5}$ and $(\alpha h\nu)^2$, respectively, where $h\nu$ is the incident photon energy.
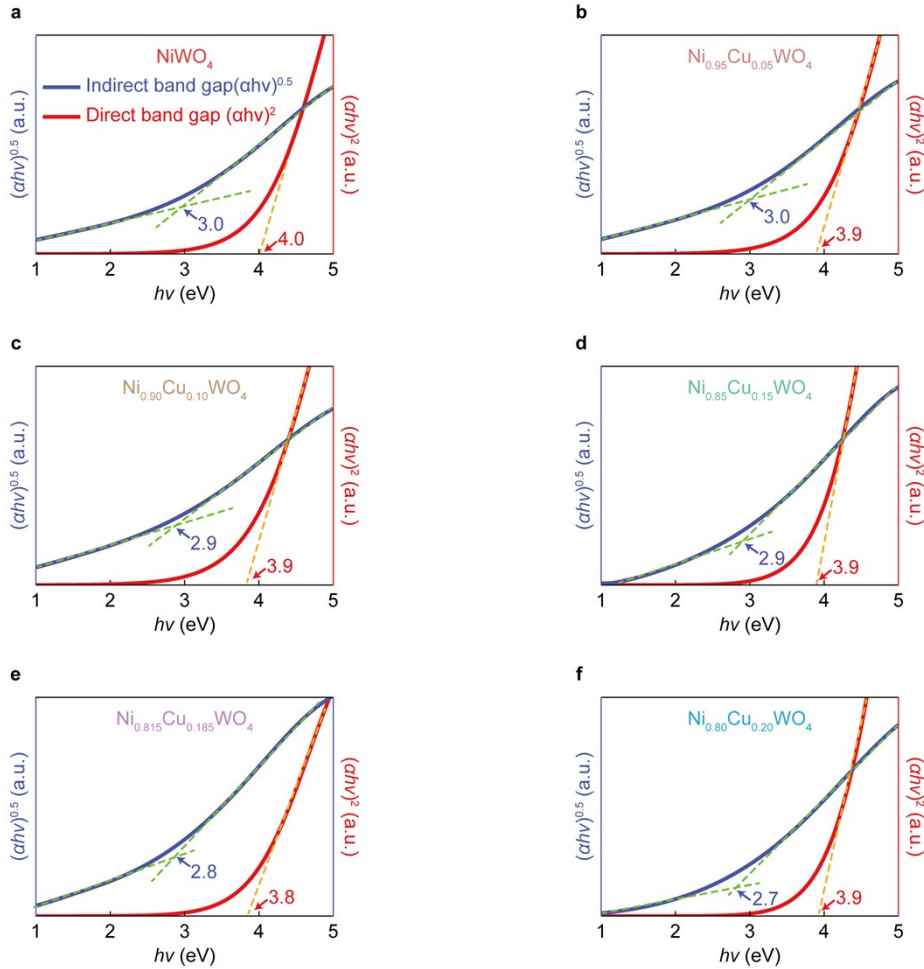

Figure S6. Optical absorption spectra of $Ni_{1-x}Cu_xWO_4$ samples with (a) $x = 0.00$, (b) $x = 0.05$, (c) $x = 0.10$, (d) $x = 0.15$, (e) $x = 0.185$, and (f) $x = 0.20$. All the resultant band gap values are plotted in Fig. 2h in the main manuscript.

S8. Schematic band diagrams of $Ni_{1-x}Cu_xWO_4$

The schematic band diagrams of $Ni_{1-x}Cu_xWO_4$ with $x = 0.15$, 0.185, and 0.20 (the energetic levels measured by UV-vis and UPS) are provided in Figure S7. As shown from Figure S7, the optical band gap as well as the work function level vary minimally with x.
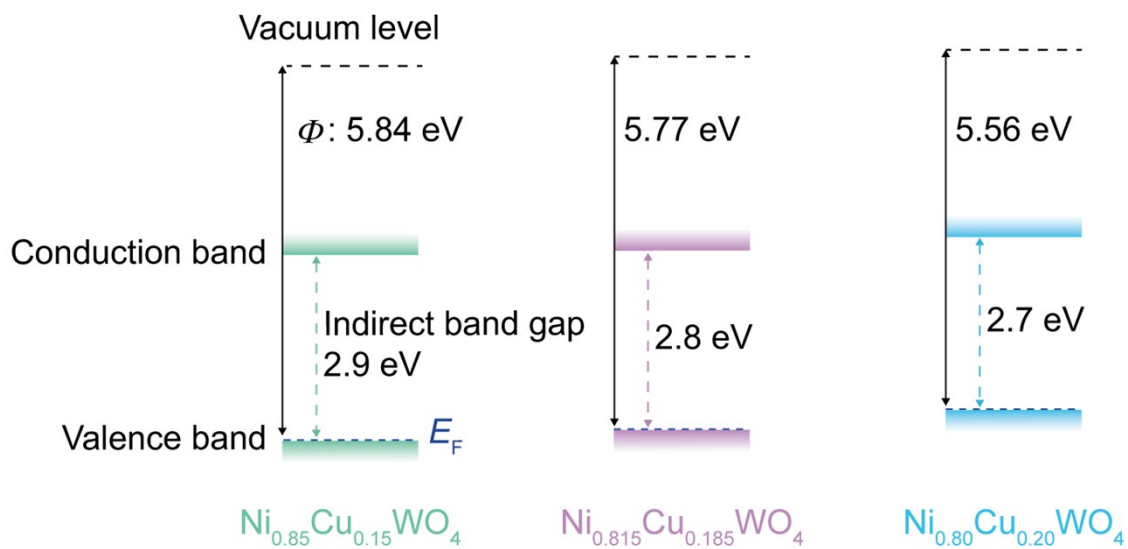

Figure S7. The band energetics of $Ni_{1-x}Cu_xWO_4$ with (a) $x = 0.15$, (b) $x = 0.185$, and (c) $x = 0.20$, determined by UV-vis and UPS results.

S9. Valence band spectra for $Ni_{1-x}Cu_xWO_4$ samples

Figure S8 displays valence band spectra for $Ni_{1-x}Cu_xWO_4$ samples with $x = 0.15$, 0.185, and 0.20. Regadless of x, all spectra show similar qualitative features of storongly correlated oxides whose d bands are partially occupied with a high number of electrons (such as d^7, d^8, and d^9) as observed from Co_3O_4, CoO, NiO, and CuO. [S4]
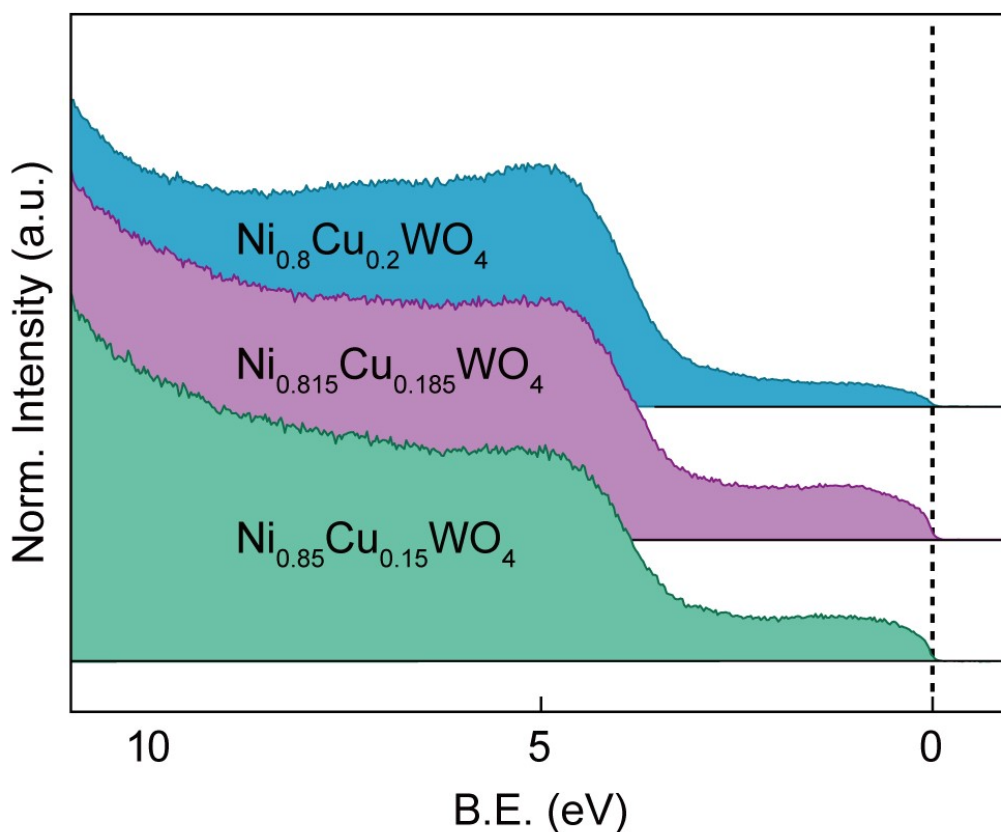

Figure S8. Valence band spectra of the $Ni_{1-x}Cu_xWO_4$ samples with respect to the binding energy (B.E.) for $x = 0.15$, 0.185, and 0.2.

S10. Performance and properties comparison of $Ni_{0.815}Cu_{0.185}WO_4$ with other representative *p*-TCOs

Table S3. Comparison of performance and physical properties of $Ni_{0.815}Cu_{0.185}WO_4$ and other representative *p*-TCOs. We note that our $Ni_{0.815}Cu_{0.185}WO_4$ are sintered polycrystalline bulk samples while the others materials were optimized thin films with relatively high crystallinity.

Material	μ_H (cm^2/Vs)	p (cm^{-3})	E_g (eV)	Φ (eV)
$Ni_{0.815}Cu_{0.185}WO_4$	**0.74 (300 K)** **6.98 (200 K)**	**1.11 × 10^{15} (300 K)** **2.62 × 10^{12} (200 K)**	**2.8 (indirect)** **3.8 (direct)**	**5.77**
CuO[S5]	6	1.00 × 10^{15}	1.4	4.7 − 5.5[S6]
Cu$_2$O[S7]	60	1.00 × 10^{15}	2.0	5.00[S6]
SnO[S8]	3.9	5.60 × 10^{15}	2.7	5.2[S9]
Li:NiO[S10]	0.025	6.12 × 10^{21}	3.65	4.85
CuAlO$_2$[S11]	10.4	1.30 × 10^{17}	3.5	5.25[S12]
LaCuOS[S13]	0.2	2.00 × 10^{15}	3.1	4.8
ZnCo$_2$O$_4$[S14]	0.2	1.37 × 10^{20}	2.63	4.52[S15]
ZnRh$_2$O$_4$[S16]	0.09	1.40 × 10^{20}	2	4.2

S11. Comparison of various U_{Ni} and U_{Cu}

Figures S9 and S10 show the evolution of the band structure and partial density of states (PDOS) for $NiWO_4$ and $Cu_xNi_{1-x}WO_4$ with various U_{Ni} and U_{Cu}, respectively. One can observe the splitting of the *d-d* gap with increasing not only U_{Ni} but also U_{Cu} demonstrating the strongly correlated nature of $NiWO_4$ and $Ni_{1-x}Cu_xWO_4$.
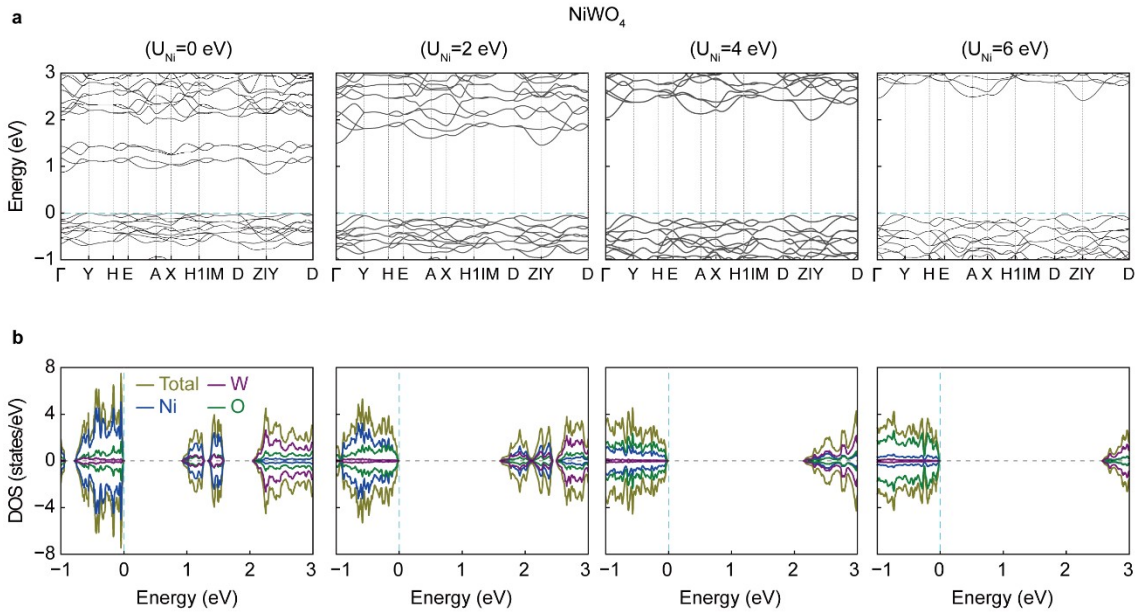

Figure S9. (a) Band structure and (b) PDOS plots for $NiWO_4$ with various U_{Ni}.

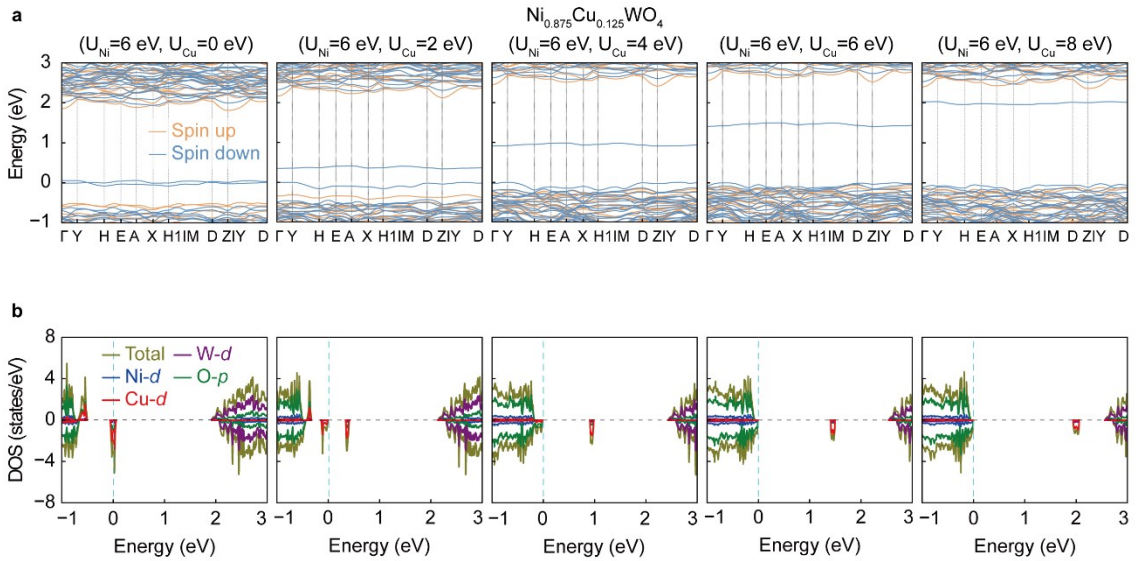**Figure S10.** (a) Band structure and (b) PDOS plots for $Ni_{1-x}Cu_xWO_4$ with various U_{Cu}.

S12. Possible origins for the encouraged polarities in $Ni_{1-x}Cu_xWO_4$ samples

As a reason for the increase in dielectric constant, we suspect that the increased distance especially in Ni–O bonding with increasing Cu contents (x) (see Figure S11 below) is responsible for the magnitude of electric dipole moment. From the definition of $p = qd$ (where, p is the electric dipole moment, q is charge amount for each dipole element, and d is the distance between dipole elements), p is proportional to d that should be bonding length between Ni and O. From the fact that the less valent Cu^{1+}/Cu^{2+} than Ni^{2+}/Ni^{3+} substitution could induce the increment on Ni^{3+} state rather than Ni^{2+} one, q could also increase as Cu-substitution as depicted in the charge density plot. (Fig. 3i and 3j) In addition, it could consider a large defect complex-dipole cluster formation as observed from the colossal permittivity materials as another origin candidate for our $Ni_{1-x}Cu_xWO_4$, [S17] but it should be supported by in-depth defect analysis as a further study.
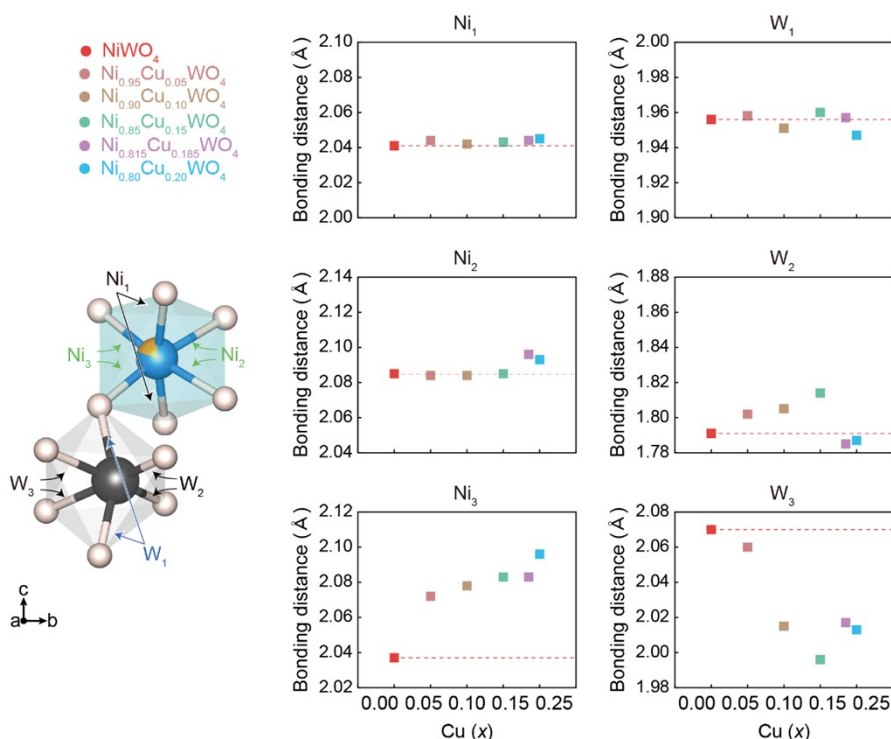

Figure S11. Bonding distance plots for each metals-oxides as a function of Cu contents (x).

15

S13. Detailed description on the enhanced polaronic conduction mechanism

The carrier transport in a transition metal oxide is typically governed by polaronic hopping conduction behavior (that means carrier hopping between the localized potential well, self-generated by displacing the surrounding ions) originating from the narrow d-band based valence band maximum. [S18, S19] In this model, the range of action of the electron-phonon interaction is a critical parameter to determine the hole hopping efficiency related to the hole carrier mobility. Figure S12 shows the representation and properties of "small" and "large" polarons. [S19] As illustrated in Fig. S12, the range (radius) of polaron increases as the degree of electron-phonon interaction decreases, which is representable in terms of the dimensionless electron-phonon interaction α, decreases, resulting in the promoted carrier mobility with band-like temperature dependency. (distinct from the thermally activated behavior as shown from Fig. 2e in the main manuscript) From the definition of $\alpha = e^2 \left(\dfrac{1}{\varepsilon_\infty} - \dfrac{1}{\varepsilon_0} \right) \sqrt{\dfrac{m}{2\omega_0}}$, it suppresses as the dielectric constant, ε that represents the ionic polarizability, increases, thus the promoting ionic polarizability plays a critical role in the hole mobility enhancement.
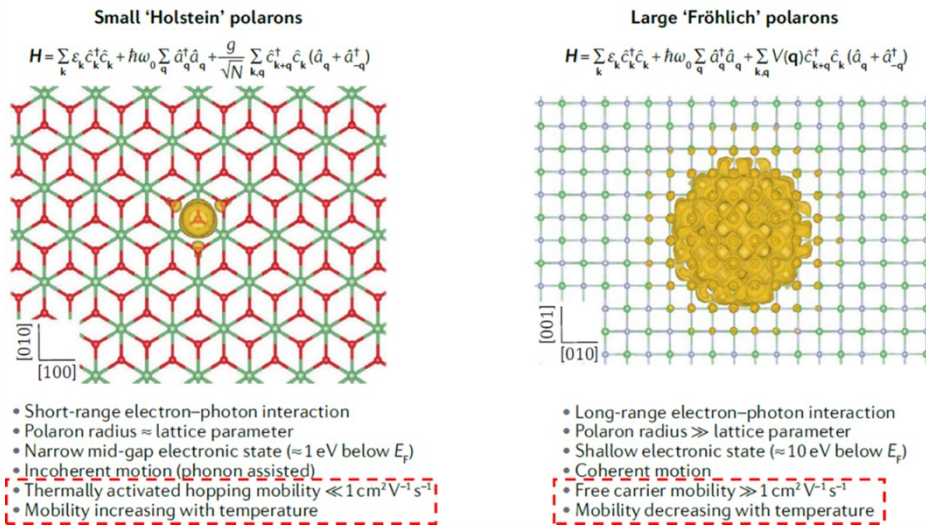

Figure S12. Comparison between "small" and "large" polaron. [Reproduced from Ref.

S19] The parameters relating carrier mobility are highlighted by red-dashed lines.

S14. Electrical properties for $Ni_{0.815}Cu_{0.185}WO_4$ thin films

Figure S13 shows the electrical properties measured by the transmission line model (TLM) method for sputtered $Ni_{0.815}Cu_{0.185}WO_4$ thin films with a 30 nm and 100 nm thickness deposited under Ar only and Ar/O_2 mixture working pressure condition, respectively. As shown in Figure S13, the 30 nm-thick film deposited under Ar only condition exhibits much lower channel resistivity (ρ_{ch}) compared to that of the 100 nm-thick film deposited under Ar/O_2 mixture gas ambient. Note that the sputtering deposition rate of the two films is quite different, being 8.3 and 1.4 nm/min for the Ar (30 nm) and Ar/O_2 (100 nm) films, respectively. Since it is well known that a cation vacancy is a shallow and efficient acceptor, while an oxygen interstitial is a deep and inefficient one for hole carrier doping, [Refs. S20-S22] the more conductive 30 nm-thick $Ni_{0.815}Cu_{0.185}WO_4$ film deposited in Ar only condition may exhibit a more non-stoichiometric nature containing high cation vacancy concentration as also inferred from the inferior visible transmittance. Because deep and relatively inactive oxygen interstitial is favoured to be formed under a high oxygen partial pressure condition, Ar/O_2 mixed ambient with a lower deposition rate could induce a more stoichiometric balance nature containing higher oxygen interstitial concentration, resulting in higher resistivity as well as higher transmittance. (refer to Fig. 4b) In addition, from the fact that the definite Hall signal did not detected from the thin film samples, their amorphous nature influces on the decrement of μ_H mainly owing to the more structural disorders compared to the polycrystalline bulk samples. [S18, S23]
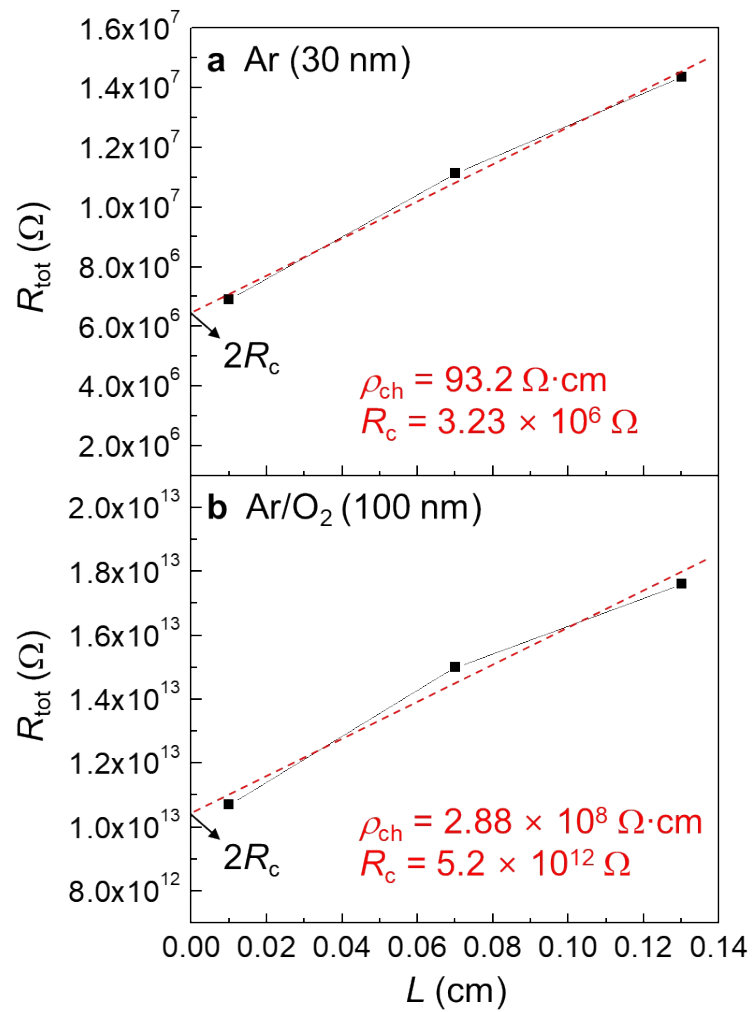
Figure S13. Measured ρ_{ch} values by TLM method for (a) 30 nm- and (b) 100 nm-thick thin films deposited under different working gas pressure condition. R_c denotes contact resistance between thin film and Au electrode.

S15. QD-LED device structure and energy band diagram

Figure S14a shows the schematic of the QD-LED device structure adopting $Ni_{0.815}Cu_{0.185}WO_4$ as the hole transporting layer (HTL). The high-resolution cross-sectional transmission electron microscopy (HR-TEM) image is also shown to visualize the device layer order as well as each film thickness. Figure S14b depicts the energy band digram alignment of the QD-LED containing the $Ni_{0.815}Cu_{0.185}WO_4$ HTL under an assumption of invariant work function in amorphous thin film surface as other TCOs did. [S24, S25]
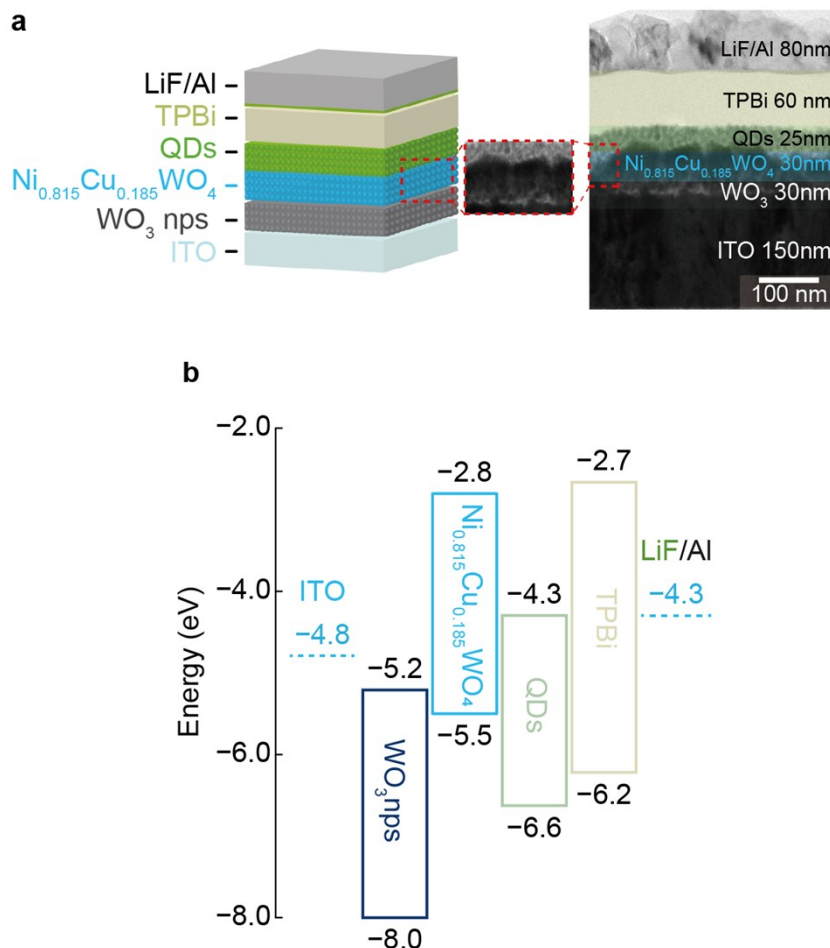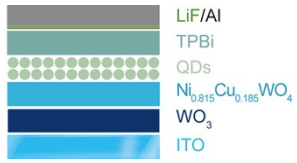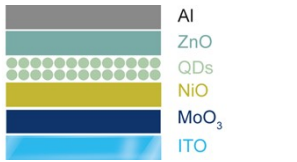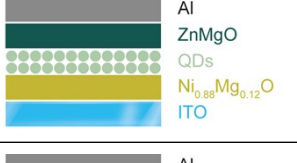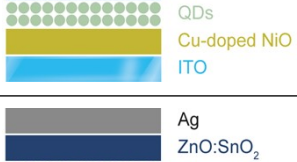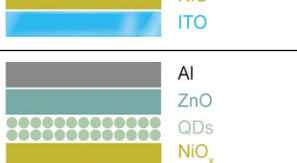

Figure S14. (a) Schematic device structure of our QD-LED and corresponding cross-sectional HR-TEM image. (b) Energy band diagram picture for all layers composing the QD-LED device.

S16. Device performances of QD-LED adopting various inorganic HTLs.

Table S4. The maximum luminescence and current efficiency performances of our QD-LED and other reported in the literature adopting diverse inorganic HTLs under similar stacking structure using CdSe-based QD as the emission layer.

	Luminescence (cd/m^2)	Current efficiency (cd/A)	Device structure
This work	**16258**	**8.67**	LiF/Al / TPBi / QDs / Ni$_{0.815}$Cu$_{0.185}$WO$_4$ / WO$_3$ / ITO
Yang *et al.*[S26]	5200	3.4	Al / ZnO / QDs / NiO / MoO$_3$ / ITO
Jiang *et al.*[S27]	27000	4.5	Al / ZnMgO / QDs / Ni$_{0.88}$Mg$_{0.12}$O / ITO
Zhang *et al.*[S28]	2285	1.18	Al / ZnO / QDs / Cu-doped NiO / ITO
Caruge *et al.*[S29]	1950	0.064	Ag / ZnO:SnO$_2$ / QDs / NiO / ITO
Ji *et al.*[S30]	~6000	3.8	Al / ZnO / QDs / NiO$_x$ / ITO

S17. Device performances of oxide-based p/n junction diodes.

Table S5. Performance comparison of our p-$Ni_{0.815}Cu_{0.185}WO_4$/n-IGZO diode and other oxide-based p/n junction devices.

Materials		V_{on} (V)	on/off ratio	Ideality factor	Operating voltage (V)
p	n				
a-Ni$_{0.815}$Cu$_{0.185}$WO$_4$	**a-IGZO**	**2.6**	**5.6×10^4**	**3.14**	**±3**
CuO	ZnO[S31]	0.66	450	-	±1.25
Cu$_2$O	IGZO[S32]	0.44	3.4×10^4	1.4	±1.2
SnO	ZnO[S33]	3	12	11.2	±4.5
SnO	SnO$_2$[S34]	3.27	10^3	3.27	±3
SrCu$_2$O$_2$	ZnO[S35]	0.3 – 0.6	80	1.62	±1.5
Ca:CuYO$_2$	Al:ZnO[S36]	0.4 – 0.8	190	-	±3
CuAlO$_2$	ZnO[S37]	0.5	90	-	±1.5
LaCuOSe	a-IGZO[S38]	6	10	-	±8
a-ZnRh$_2$O$_4$	a-IGZO[S39]	2.1	10^3	2.3	±5
a-ZnCo$_2$O$_4$	a-IGZO[S40]	2.5	10^2	-	±7
ZnCo$_2$O$_4$	Mg:In$_2$O$_3$[S41]	-	10^3	2	±1

S18. Energy band diagram picture for p-$Ni_{0.815}Cu_{0.185}WO_4$/n-IGZO diode

Figure S15 depicts the the energy band digram alignment of our oxide p/n junction diode containing p-$Ni_{0.815}Cu_{0.185}WO_4$ and n-IGZO layers. The relatively large built-in potential value of 0.9 V is formed under an assumption of invariant work function in amorphous thin film surface as other TCOs did, [S24, S25] resulting in highly rectifying $I - V$ behabiour.
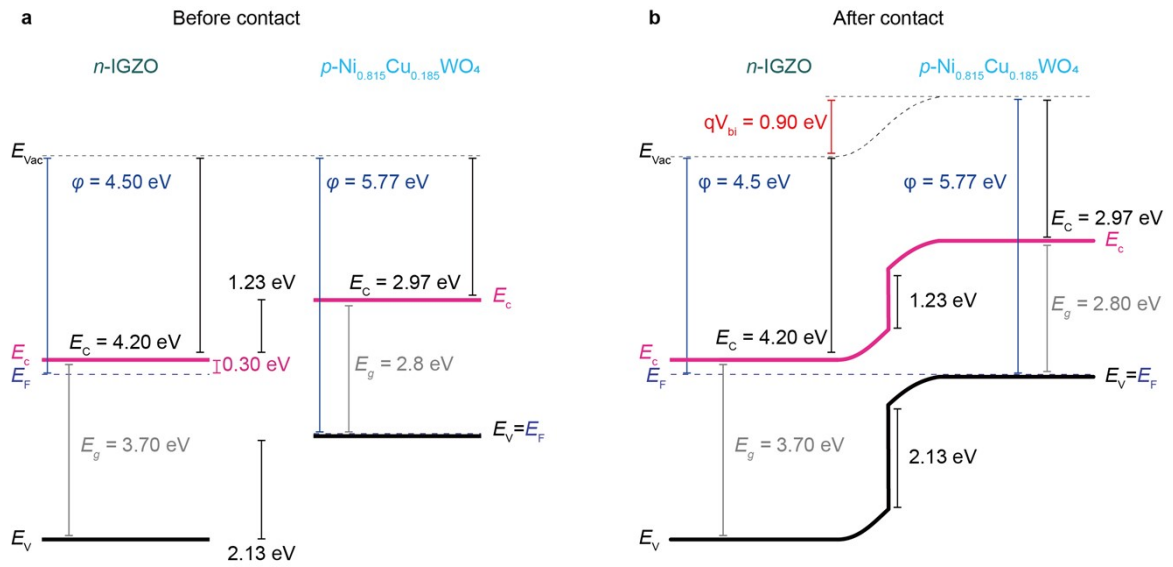

Figure S15. Equilibrium energy band diagram picture for our p-$Ni_{0.815}Cu_{0.185}WO_4$/n-IGZO diode. The conduction band minimum (E_c) and Fermi level (E_f) of n-IGZO are from Ref. S42.

References

S1. Pronsnikov, M. A., Davydov, V. Y., Smirnov, A. N., Volkov, M. P. & Pisarev, R.V. Lattice and spin dynamics in a low-symmetry antiferromagnet $NiWO_4$. *Phys. Rev. B* **96**, 014428 (2017).

S2. Lee, K. *et al.* Over 40 cd/A efficient green quantum dot electroluminescent device comprising uniquely large-sized quantum dots. *ACS Nano* **8**, 4893-4901 (2014).

S3. Kuzmin, A., Kalinko, A. & Evarestov, R. A. First-principles LCAO study of phonons in $NiWO_4$. *Cent. Eur. J. Phys.* **9**, 502-509 (2011).

S4. Greiner, M. T. *et al.* Universal energy-level alignment of molecules on metal oxides. *Nat. Mater.* **11**, 76-81 (2012).

S5. Shen, Y. L., Guo, M. L., Xia, X. H. & Shao, G. S. Role of materials chemistry on the electrical/electronic properties of CuO thin films. *Acta Mater.* **85**, 122-131 (2015).

S6. Deuermeier, J. *et al.* Visualization of nanocrystalline CuO in the grain boundaries of Cu_2O thin films and effect on band bending and film resistivity. *APL Mater.* **6**, 096103 (2018).

S7. Shogo, I., Takahiro, M. & Katsuhiro, A. Thin-film deposition of Cu_2O by reactive radio-frequency magnetron sputtering. *Jpn. J. Appl. Phys.* **39**, L786 (2000).

S8. Liang, L. Y. *et al.* The structural, optical and electrical properties of Y-doped SnO thin films and their p-type TFT application. *J. Phys. D: Appl. Phys.* **45**, 085101 (2012).

S9. Doh, W. H., Jeong, W., Lee, H., Park, J. & Park, J. Y. Work function engineering of SnO single crystal microplates with thermal annealing. *Nanotech.* **27**, 335603

(2016).

S10. Zhang, J. Y. *et al.* Electronic and transport properties of Li-doped NiO epitaxial thin films. *J. Mater. Chem. C* **6**, 2275-2282 (2018).

S11. Kawazoe, H. *et al.* P-type electrical conduction in transparent thin films of $CuAlO_2$. *Nature* **389**, 939-942 (1997).

S12. Long, Y. *et al.* Enhanced spectral response of ZnO-nanorod-array-based ultraviolet photodetectors by alloyng non-isovalent Cu-O with $CuAlO_2$ *p*-type layer. *Nanomaterials* **13**, 1472 (2023).

S13. Hiramatsu, H. *et al. J. Appl. Phys.* Intrinsic excitonic photoluminescence and band-gap engineering of wide-gap *p*-type oxychalcogenide epitaxial films of *Ln*CuO*Ch* (*Ln* = La, Pr, and Nd; *Ch* = S or Se) semiconductor alloys. **94**, 5805-5808 (2003).

S14. Kim, H. J. *et al.* Electrical and magnetic properties of spinel-type magnetic semiconductor $ZnCo_2O_4$ grown by reactive magnetron sputtering. *J. Appl. Phys.* **95**, 7387-7389 (2004).

S15. Jheng, B. R., Chiu, P. T., Yang, S. H. & Tong, Y. L. Using $ZnCo_2O_4$ nanoparticles as the hole transport layer to improve long term stability of perovskite solar cells. *Sci. Rep.* **12**, 2921 (2022).

S16. Kamiya, T. *et al.* Electrical properties and structure of p-type amorphous oxide semiconductor $xZnO \cdot Rh_2O_3$. *Adv. Func. Mater.* **15**, 968-974 (2005).

S17. Austin, I. G. & Mott, N. F. Polarons in crystalline and non-crystalline materials. *Adv. Phys.* **50**, 757-812 (2001).

S18. Franchini, C., Reticcioli, M., Setvin, M. & Diebold, U. Polarons in materials. *Nat. Rev. Mater.* **6**, 560-586 (2021).

S19. Robertson, J. & Zhang, Z. Doping limits in *p*-type oxide semiconductors. *MRS Bull.* **46**, 1037-1043 (2021).

S20. Oba, F., Choi, M., Togo, A., Seko, A., & Tanaka, I. Native defects in oxide semiconductors: a density functional approach. *J. Phys.: Condens. Matter*, **22**, 384211 (2010).

S21. Volnianska, O. & Boguslawski, P. Caculated properties of point native defects and p-type conductivity of $ZnRh_2O_4$. *J. Appl. Phys.* **114**, 033711 (2013).

S22. Yang, X. *et al.* High-efficiency all-inorganic full-colour quantum dot light-emitting diodes. *Nano Energy*, **46**, 229-233 (2018).

S23. Jiang, Y. *et al.* All-inorganic quantum-dot light-emitting diodes with reduced exciton quenching by a MgO decorated inorganic hole transport layer. *ACS Appl. Mater. Interfaces* **11**, 11119-11124 (2019).

S24. Zhang, Y. & Zhao, L. Enhanced electroluminescence performance of all-inorganic quantum dot light-emitting diodes: A promising candidate for hole transport layer of Cu-doped NiO nanocrystals. *J. Mater. Res.* **34**, 2757-2764 (2019).

S25. Caruge, J. M., Halpert, J. E., Wood, V., Bulović, V. & Bawendi, M. G. Colloidal quantum-dot light-emitting diodes with metal-oxide charge transport layers. *Nat. Photonics* **2**, 247-250 (2008).

S26. Ji, W. *et al.* Ultrasonic spray processed, highly efficient all-inorganic quantum-dot light-emitting diodes. *ACS Photonics* **4**, 1271-1278 (2017).

S27. Saji, K. J., Populoh, S., Tiwari, A. N. & Romanyuk, Y. E. Design of p-CuO/n-ZnO heterojunctions by rf magnetron sputtering. *Phys. Status Solidi A* **210**, 1386-1391 (2013).

S28. Chen, W. C. *et al.* Room-temperature-processed flexible n-InGaZnO/p-Cu_2O

heterojunction diodes and high-frequency diode rectifiers. *J. Phys. D: Appl. Phys.* **47**, 365101 (2014).

S29. Snanl, K. C. & Jayaraj, M. K. Growth and characterization of tin oxide thin films and fabrication of transparent p-SnO/n-ZnO p–n hetero junction. *Mater. Sci. Eng. B* **178**, 816-821 (2013).

S30. Wang, Z. *et al.* Transparent SnO–SnO_2 p–n junction diodes for electronic and sensing applications. *Adv. Mater. Interfaces* **2**, 1500374 (2015).

S31. Kudo, A. *et al.* Fabrication of transparent *p-n* heterojunction thin film diodes based entirely on oxide semiconductors. *Appl. Phys. Lett.* **75**, 2851-2853 (1999).

S32. Jayaraj, M. K., Draeseke, A. D., Tate, J. & Sleight, A. W. p-Type transparent thin films of $CuY_{1-x}Ca_xO_2$. *Thin Solid Films* **397**, 244-248 (2001).

S33. Tonooka, K., Bando, H. & Aiura, Y. Photovoltaic effect observed in transparent p–n heterojunctions based on oxide semiconductors. *Thin Solid Films* **445**, 327-331 (2003).

S34. Hiramatsu, H. *et al.* Excitonic blue luminescence from *p*-LaCuOSe/*n*-$InGaZn_5O_8$ light-emitting diode at room temperature. *Appl. Phys. Lett.* **87**, 211107 (2005).

S35. Narushima, S. *et al.* A p-Type amorphous oxide semiconductor and room temperature fabrication of amorphous oxide p–n heterojunction diodes. *Adv. Mater.* **15**, 1409-1413 (2003).

S36. Kim, S. *et al.* Room temperature deposited oxide p-n junction using p-type zinc-cobalt-oxide. *J. Appl. Phys.* **107**, 103538 (2010).

S37. Wenckster, H. v. *et al.* pn-Heterojunction diodes with n-type In_2O_3. *Adv. Electron. Mater.* **1**, 1400026 (2015).

S38. Lee, D. H., Nomura, K., Kamiya, T. & Hosono, H. Diffusion-limited a-IGZO/Pt Schottky junction fabricated at 200 ^{o}C on a flexible substrate. *IEEE Elec. Dev. Lett.* **32**, 1695-1697 (2011).